

Dynamics and Assembly of the Cytolethal Distending Toxin

Xin Hu and C. Erec Stebbins*

Laboratory of Structural Microbiology, The Rockefeller University, New York, New York 10021

ABSTRACT The cytolethal distending toxin (CDT) is a widespread bacterial toxin that consists of an active subunit CdtB with nuclease activity and two ricin-like lectin domains, CdtA and CdtC, that are involved in the delivery of CdtB into the host cell. The three subunits form a tripartite complex that is required to achieve the fully active holotoxin. In the present study we investigate the assembly and dynamic properties of the CDT holotoxin using molecular dynamics simulations and binding free energy calculations. The results have revealed that CdtB likely adopts a different conformation in the unbound state with a closed DNA binding site. The two characterized structural elements of the aromatic patch and groove on the CdtA and CdtC protein surfaces exhibit high mobility, and free energy calculations show that the heterodimeric complex CdtA-CdtC, as well as the CdtA-CdtB and CdtB-CdtC sub-complexes are less energetically stable as compared to the binding in the tripartite complex. Analysis of the dynamical cross-correlation map reveals information on the correlated motions and long-range interplay among the CDT subunits associated with complex formation. Finally, the estimated binding free energies of subunit interactions are presented, together with the free energy decomposition to determine the contributions of residues for both binding partners, providing insight into the protein–protein interactions in the CDT holotoxin. *Proteins* 2006;65:843–855. © 2006 Wiley-Liss, Inc.

Key words: cytolethal distending toxin (CDT); protein–protein interaction; dynamical cross-correlation map (DCCM); binding free energy; molecular mechanics-generalized born surface area (MM-GBSA)

INTRODUCTION

The cytolethal distending toxin (CDT) is a unique bacterial toxin that has the ability to activate the DNA damage checkpoint responses, causing irreversible cell cycle arrest or apoptosis in intoxicated cells.^{1–3} CDT has been found in a variety of bacterial pathogens such as *Campylobacter jejunii*, *Campylobacter fetus*, *Shigella* spp., *Haemophilus ducreyi*, *Actinobacillus actinomycescomitans*, *Helicobacter hepaticus*, and certain pathogenic strains of *Escherichia coli*.^{1,2,4} These gram-negative bacteria have been implicated in a wide range of

human diseases, and several studies have shown that CDT as a potential virulence factor may play an important role in disease progression and immunosuppression.^{5–7}

CDT cytotoxicity is associated with the products of an operon that encodes three proteins: CdtA, CdtB, and CdtC with molecular masses of 23, 29, and 21 kDa, respectively.^{8,9} CdtB is the enzymatically active subunit with nuclease activity and exhibits sequence similarity with the deoxyribonuclease (DNase I) family.¹⁰ CdtA and CdtC are the binding elements for target cells and necessary for the intracellular delivery of CdtB.^{11,12} All three of these protein subunits are generally required to constitute the fully active holotoxin.^{13,14} It has been proposed that the CDT holotoxin is internalized into target cells by means of receptor-mediated endocytosis, while the CdtB subunit is transported from the ER to the cytosol by retrotranslocation, and finally to the nucleus where it activates DNA damage checkpoints.^{2,15,16}

The recently determined crystal structure of CDT from *H. ducreyi* has revealed a wealth of knowledge on the molecular basis of the assembly and function of the holotoxin.¹⁷ CDT possesses a ternary structure with the active CdtB subunit bound to two ricin-like lectin domains, CdtA and CdtC [Fig. 1(A)]. All three subunits interact intimately with each other, forming three extensive globular protein–protein interfaces. CdtA and CdtC each have extended, non-globular polypeptides at their N- and C-termini, and in both proteins these regions interact with other elements of the holotoxin to cement the assembly of the ternary complex. The tripartite structure of CDT delineates several distinguishing features that generate functional hypotheses. One is the N-terminus of CdtC that extends to the active site of CdtB and sterically occludes the active site, serving an auto-inhibitory role for the holotoxin in vitro. CdtA and CdtC together contribute towards the formation of a large aromatic patch and an adjacent deep groove on the protein

The Supplementary Material referred to in this article can be found at <http://www.interscience.wiley.com/jpages/0887-3585/suppmat/>

Grant sponsor: National Institute of Allergy and Infectious Disease; Grant number: 1U19AI056510; Grant sponsor: The Rockefeller University.

*Correspondence to: C. Erec Stebbins, Laboratory of Structural Microbiology, The Rockefeller University, New York, NY 10021. E-mail: stebbins@rockefeller.edu

Received 15 December 2005; Revised 4 May 2006; Accepted 13 July 2006

Published online 10 October 2006 in Wiley InterScience (www.interscience.wiley.com). DOI: 10.1002/prot.21167

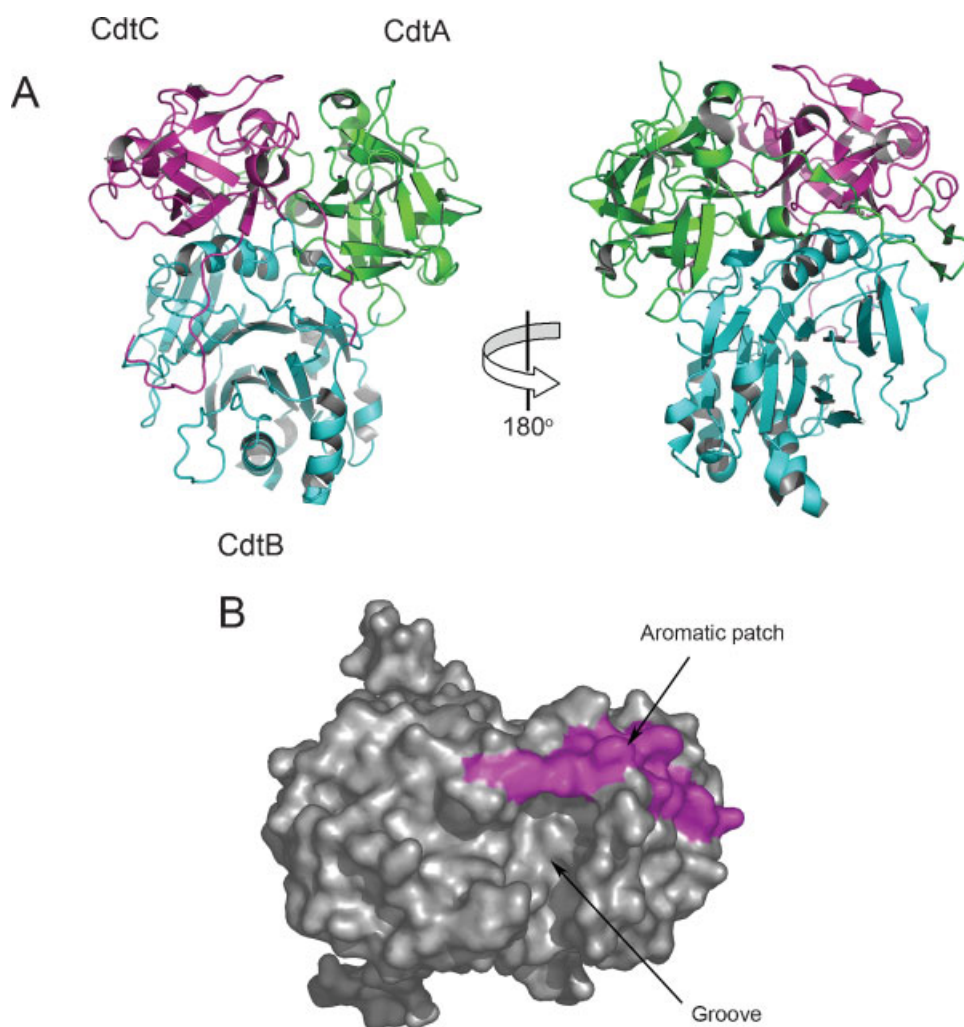


Fig. 1. (A) Ribbon representations of the CDT structure (PDB: 1SR4) shown in green (CdtA), cyan (CdtB), and purple (CdtC), respectively. The orientation in the right-hand panel corresponds to a 180° clockwise rotation around the vertical axis compared to the orientations in the left-hand panel. (B) Surface representations of CdtA-CdtC heterodimeric complex. The aromatic patch is colored in magenta.

surface, which play an important role in the binding to host cell surface [Fig. 1(B)].¹¹ A mutant *H. ducreyi* holotoxin with deletion of the CdtC N-terminus possesses DNase activity in vitro and is toxic in vivo, while the wild-type holotoxin shows no nuclease activity in vitro.¹⁷ Studies have also shown that CdtA and CdtC are each able to bind to the cell surface, but the binding affinities increase significantly when both components are combined.^{12,14} Mutagenesis of the CdtA and CdtC residues in the aromatic patch renders the holotoxin inactive in cellular assays and impairs cell surface binding, but the ternary complex stability is unimpaired.^{11,17}

The availability of the CDT crystal structure has opened new opportunities to study the assembly, stability, and functional aspects of the CDT holotoxin at the atomic level using computational approaches. Molecular dynamics (MD) simulations and binding free energy calculations have been extensively applied in studies of

protein–ligand and protein–protein interactions.^{18,19} Recently developed methods such as MM-PB(GB)SA for the estimation of binding free energy, and further examination of contributions of individual residues to the binding affinity, provide a useful means to investigate the energetics and structural basis of protein–protein interactions, as well as application in structure-based drug design.^{20–23} CDT functions in a manner that is closely associated with the complex formation of three structural components. Detailed modeling studies of dynamic behavior of the CDT structure and the nature of the subunit interactions should help in identifying the elements essential for the holotoxin assembly and stability in aqueous solution, and shed light on the related functional aspects of this unique toxin. In addition, in the absence of structural information on the catalytic subunit CdtB as well as the complex with DNA, computational prediction for the unbound CdtB and binding to

the substrate DNA is critical in understanding of the catalytic mechanism of CDT intoxication.

In the present work we carried out 10 ns of MD simulations on the CDT holotoxin in explicit solvent. MD simulations of the unbound subunits (CdtA, CdtB, and CdtC), the separate heterodimeric sub-complexes (CdtA-CdtC, CdtB-CdtA, and CdtB-CdtC), as well as the modeled CdtB-DNA complex were also conducted to investigate the stability and possible conformational changes associated with complex formation and disassembly in different states. A dynamical cross-correlation map (DCCM) was calculated for a detailed analysis of the correlated motions and long-range interplay of the binding partners with respect to each other. To evaluate the energetic changes in the complex assembly, absolute binding free energies were calculated for the sub-complex in the separate and complexed states. The predicted binding free energies between CdtA, CdtB, and CdtC and the results of binding energy decomposition for the contributions of residues to the binding affinity provides information on the assembly and nature of subunit interactions that should guide further experimental investigation.

METHODS

MD Simulations

Coordinates of the CDT tripartite complex for the MD simulations were obtained from the Protein Data Bank (PDB entry 1SR4). The initial structures of each subunit (CdtA, CdtB, and CdtC) and sub-complexes (CdtA-CdtC, CdtB-CdtA, and CdtB-CdtC) were directly obtained from the tripartite complex, and the averaged structures generated from the MD trajectory in equilibrium state were used as representatives for structural analysis. The CdtB/DNA complex was modeled by positioning double-stranded DNA (d(GGTATACC)) into the CdtB active site as aligned with DNase I/DNA complex (PDB entry 1DNK).²⁴ The docked CdtB/DNA complex was subjected to a full energy minimization to release any steric clash. The energy minimizations were carried out employing modeling package Sybyl 7.0,²⁵ MMFF94s force field was applied with 0.05 kcal/mol Å convergence and 5000 steps using the Powell method.²⁶

MD simulations were carried out using the SANDER module of the AMBER 8.0 package and the Parm99 force field.²⁷ All systems were solvated by a cubic box of TIP3P water molecules,²⁸ which extended 12 Å from protein atoms. The solvated protein systems were neutralized by counter ions and subjected to a thorough minimization prior to MD simulations. The minimization was performed on two steps: first the water molecules were minimized while holding solute frozen (1000 steps using the steepest descent algorithm), then the whole system was minimized with 5000 steps of conjugate gradient to remove close contacts and to relax the system. All the MD runs were set up using the same protocol. Bond lengths involving bonds to hydrogen were constrained with SHAKE²⁹ and the time step for all MD simulations

was 2 fs. A non-bonded cutoff of 10 Å was used, and the non-bonded pair list was updated every 25 times steps. Periodic boundary conditions were applied to simulate a continuous system. The particle mesh Ewald method was employed to calculate the long-range electrostatic interactions.³⁰ The simulated system was first subjected to a gradual temperature increase from 0 to 300 K over 20 ps, and then equilibrated for 500 ps at 300 K, followed by the production run of 10 ns length in total for the tripartite complex and the unbound CdtB, and 8 ns for other CDT systems. Constant temperature and pressure (300 K/1 atm) were maintained using the Berendsen coupling algorithm³¹ with time constant for heat bath coupling of 0.2 ps.

The resulting trajectories were analyzed using the PTRAJ module of AMBER 8.0 package. All counter ions and water molecules were stripped from the MD structures. The root-mean-square deviations (RMSDs) of the backbone atoms of CDT were calculated from the trajectories at 1 ps interval, with the initial structure as the reference. The averaged structure from 2 to 10 ns of each simulation was calculated and used as the reference to be superimposed on in the calculation of the B-factors and cross-correlation matrices. The mean-square positional fluctuations about the average structure, $\langle \Delta r_i^2 \rangle$, were calculated based on the superposition of all Cα atoms. The RMSF is related to the B-factors, which can be obtained experimentally from X-ray crystallography according to³²:

$$B_i = \frac{8\pi^2}{3} \langle \Delta r_i^2 \rangle$$

Dynamic cross-correlations of the atomic fluctuations were calculated from the differences between the Cα coordinates of the individual structures and the averaged structure over time from 2 to 10 ns of the MD trajectories. For the displacement vectors Δr_i and Δr_j for atoms i and j , respectively, the cross-correlation matrix $C(i, j)$ is given by³³:

$$C(i, j) = \frac{\langle \Delta r_i \Delta r_j \rangle}{\sqrt{\langle \Delta r_i^2 \rangle \langle \Delta r_j^2 \rangle}}$$

For completely correlated motions, $C(i, j) = 1$, and for completely anti-correlated motions, $C(i, j) = -1$. The dynamical cross-correlation map (DCCM) based on the cross-correlation matrix was plotted with the program Matlab (Mathworks Inc., Natick, MA).

Binding Free Energy Calculations

Methods of MM-PB(GB)SA on the binding free energy calculations are abundantly documented.^{20–23} Briefly, MM-PB(GB)SA estimate the (absolute) free energies of protein systems as calculated from the gas phase energies (E_{gas}), the solvation free energies ($G_{\text{solvation}}$), and the entropies (TS) according to the following equation:

$$G = E_{\text{gas}} + G_{\text{solvation}} - TS$$

E_{gas} is the sum of van der Waals energy (E_{vdw}), electrostatic energy ($E_{\text{electrostatic}}$), and the internal strain energy (E_{int}), which is associated with vibrations of covalent bonds and bond angles, rotation of single bond torsional angles.

$$E_{\text{gas}} = E_{\text{vdw}} + E_{\text{electrostatic}} + E_{\text{int}}$$

The solvation free energy, $G_{\text{solvation}}$, is approximated as the sum of the polar contribution and nonpolar contribution using a continuum representation of the solvent:

$$G_{\text{solvation}} = G_{\text{polar}} + G_{\text{nonpolar}}$$

The polar electrostatic contribution to the solvation free energy is solved with the Poisson–Boltzmann equation (G_{PB}) or generalized Born models (G_{GB}). The nonpolar hydrophobic contribution can be determined with solvent-accessible surface area (SASA). The binding free energies of protein–protein or protein–ligand interaction are then calculated by

$$\Delta G_{\text{binding}} = G_{\text{complex}} - G_{\text{protein}} - G_{\text{ligand}}$$

where G_{complex} , G_{protein} , and G_{ligand} are the calculated free energies of the complex and two subunit proteins, respectively.

In this study, we calculated the binding free energies of CDT subunit interactions using the MM-GBSA method. Although the GB model is generally used as an approximation to the PB model, many studies have shown that the MM-GBSA calculations reproduce the binding free energies of various systems in good agreement with the results calculated from the MM-PBSA method.^{34–36} A direct comparison study of these two approaches on a large protein data set has demonstrated that the overall performance of the GB model is comparable to the PB model.³⁷ In contrast to the MM-PBSA, the MM-GBSA calculations are computationally less expensive. Another intriguing property of MM-GBSA is that it allows one to decompose the contributions to binding free energies on a single residue. The direct free energy decomposition is an alternative to the “computational alanine scanning” approach,²² but without structural perturbations of the simulated system.³⁵

To calculate the mean values of binding free energies using MM-GBSA, a set of 150 snapshots was extracted from both complex and separate trajectories at 20 ps intervals from the last 3 ns of MD simulations. The molecular mechanics interaction energies were calculated with the SANDER module in the AMBER 8.0 package.²⁸ The polar contribution (G_{GB}) was calculated with the generalized Born model by Onufriev et al.³⁸ The same infinite distance cutoff (cut = 999.0) was used in both MM and GB calculations. The nonpolar contributions (G_{SA}) were estimated using the MSMS algorithm³⁹ according to the equation: $G_{\text{SA}} = \gamma \times \text{SASA} + b$ kcal

mol⁻¹. γ and b are 0.00542 kcal/mol Å⁻² and 0.92 kcal/mol, respectively, and the probe radius was set to 1.4 Å. The entropy (TS) was estimated through normal mode analysis using the NMODE module in the AMBER package. Because the calculations show very small variation, only 25 snapshots were used for entropy estimation due to the high computational demand. The snapshots were selected at equally spaced intervals (60 ps) of the last 3 ns trajectories of simulation systems. Prior to the normal analysis, thorough minimizations were carried out with a distance-dependent dielectric constant ($\epsilon = 4R_{ij}$) and no cutoff for the non-bonded interactions.

RESULTS AND DISCUSSION

Dynamics of the CDT Tripartite Complex

MD simulations were performed for the CDT tripartite complex as well as the separate heterodimeric sub-complexes and subunits, respectively. To access the quality of the simulations, we monitored the potential energy and RMSD from the initial structure throughout the MD simulations. For all simulation systems, the potential energy decreased rapidly during the first 20 ps of equilibration and reached a steady state within 500 ps of the equilibration phase (data not shown). The averaged potential energy remained constant along the trajectories, indicating that the simulations have evolved to a stable state and reasonably converged. We also inspected the total energy, the temperature, the mass density, the volume, and the energy components of the systems to ensure the stability of the systems across the entire simulations.

The dynamics of the CDT tripartite complex were evaluated by examining atomic fluctuations during the 10 ns of MD simulations. In Figure 2(A) is plotted the RMSD of backbone atoms of CDT from the trajectories as compared to the initial structure. The calculated RMSD for the entire protein shows significantly increased deviations over the time course of simulations. Since the long peptide tail of the N-terminus of CdtA (residues 18–67) is extended to the solvent without any contacts with other elements, it is expected to exhibit a higher level of mobility. Indeed, when the CdtA terminal tail is not included, the calculated RMSD is considerably decreased and remains stable [Fig. 2(A)]. The average RMSD with respect to the starting structure is less than 1.5 Å, indicating that the CDT ternary complex is rather stable, and gross features of the secondary structure and 3D folding are well maintained throughout the simulations. We also calculated the B-factors from simulations, which are often used as a measure of structural mobility of different regions of the protein. The B-factors are defined as positional fluctuations of C α atoms of CDT. As shown in Figure 2(B), the calculated B-factors are generally in agreement with the experimentally measured data. As expected, regions of the extended terminal ends of CdtA and CdtC show higher values of calculated B-factors. The CdtA N-terminus exhibits the largest motions throughout the MD simulations (calculated B-

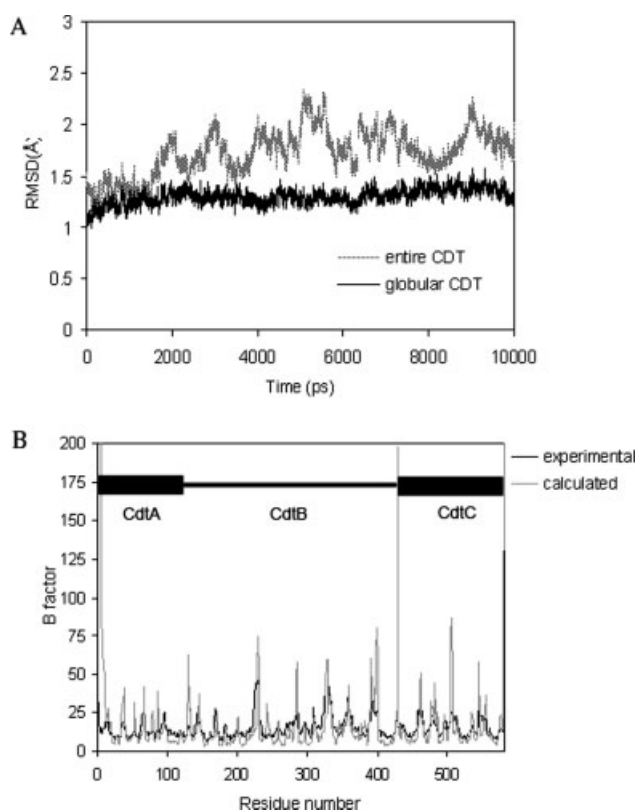


Fig. 2. (A) RMSDs of the backbone atoms for the entire CDT holotoxin (grey) and the globular regions (black) with respect to the X-ray structure over 10 ns of MD simulations. (B) Calculated B-factors of $C\alpha$ atoms of CDT from the 10 ns of MD simulations (grey line) in comparison to the experimental B-factors obtained from the crystal structure.

factors >100), but has relatively small experimental B-factors (average ~ 20) due to the formation of crystal-packing contacts within the groove on a symmetry related CdtA-CdtC protein surface.¹⁷ Similarly, the regions surrounding the groove on CdtA and CdtC show a high level of fluctuation as compared to their relatively lower B-factors in the crystal structure. Increased atomic fluctuations were also observed at several loop regions proximal to the putative DNA binding site and subunit binding interface, which are probably related to their functional aspects involving DNA catalysis and receptor binding as detailed later.

Conformational Changes of the CdtB Subunit

To probe the dynamic behavior and conformational changes of the catalytic CdtB subunit, MD simulations were carried out separately for free CdtB as well as the modeled complex with DNA. The results were compared with those of CdtB bound in the inactive tripartite complex. Figure 3(A) depicts the RMSDs calculated for the three systems over the 10 ns time course of MD simulations. All the simulation trajectories reached a stable state with an average RMSD value less than 2.0 Å. The bound CdtB in the tripartite complex and in the CdtB-

DNA complex show lower RMSD values (~ 1.0 Å), whereas unbound CdtB exhibits more flexibility (averaged RMSD ~ 2.0 Å). The large deviations of unbound CdtB with respect to the X-ray structure in the tripartite complex suggest that conformational changes probably occur due to the disassembly from CdtA and CdtC. Analysis of the atomic positional fluctuations for residues ($C\alpha$) calculated from the MD simulations reveals regional mobility in the protein structure. As shown in Figure 4, four loop regions (residues spanning 36–41, 74–91, 110–116, and 135–145) fluctuate intensely in unbound CdtB as compared to CdtB in the tripartite complex. Figure 3(B) illustrates the high flexibility of these loop regions throughout 10 ns of MD simulations. The average RMSD of these flexible loops in unbound CdtB as measured between the averaged MD structure and the X-ray structure is up to 3.0 Å, whereas it is less than 1.5 Å in the tripartite complex and in the modeled complex with DNA.

Superposition of the averaged MD structure of unbound CdtB with the crystal structure shows that, while the secondary and tertiary structure motifs of CdtB are well maintained in the simulations, significant conformational changes mainly occur with these flexible loops proximal to the DNA binding site (see Fig. 5). Loops L1(36–41) and L3(110–116) are located above the active site and make direct contacts with the CdtC N-terminus or DNA in the modeled complex, hence, likely having a direct impact on substrate binding and catalysis. Loop L2(74–91) and loop L4(135–145) are situated on the side of the putative DNA binding groove where the N-terminal peptide of CdtC extends in the tripartite complex. The distance between L2 and L4 in the bound complex is up to 17.7 Å (between the $C\alpha$ atoms of Gly85 and Val140), whereas it is only 10.8 Å in the unbound CdtB. Therefore, the two loops act as a “gate” to the active site, maintaining the DNA binding groove in a closed form in the unbound CdtB and opening up in the tripartite or DNA complex. The closure of the DNA binding site allows free CdtB to adopt a more stable conformational state, as revealed by free energy calculations. It is worth noting that loop L2 is one of the most highly conserved regions in the CDT family, and a comparison of CdtB with homologs of DNase I reveals that such a loop is absent in the DNase family (while the structural features at the DNA binding site and overall folding are highly similar between CDT and DNase I). Because of the intrinsic flexibility of this loop, it likely functions together with the partner loop L4 to facilitate substrate binding in the catalytic process.

A closer inspection of unbound CdtB indicates that significant conformational changes also occur in the DNA binding site with respect to the residues involved in substrate binding and DNA catalysis, such as the two catalytic histidines (His160, His274), the metal coordination residues (Glu66, Asp199, and Asp273), and the DNA contacting residues (Arg117, Arg144, and Asn201). These residues are found to be stabilized by a water-mediated hydrogen-bonding network in the structure of

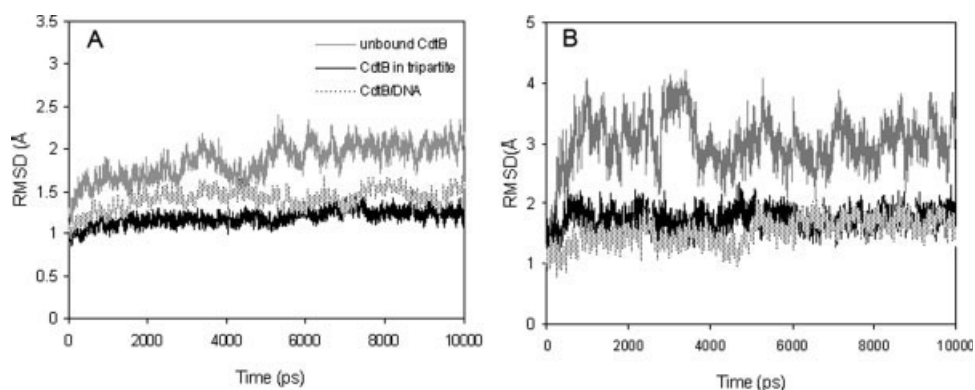


Fig. 3. (A) RMSDs of the backbone atoms for CdtB in the different states as compared to their starting structure over 10 ns of MD simulations. (B) RMSDs of the backbone atoms for loop L2 (residues 74–91) combined with L4 (residues 135–145) in the different states as compared to their starting structure during simulation.

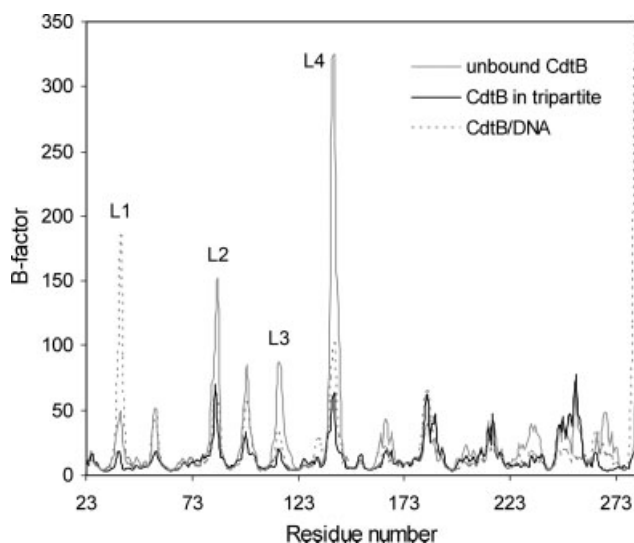


Fig. 4. Calculated B-factors of $C\alpha$ atoms of CdtB in the tripartite complex (solid black line), unbound (solid grey line), and the CdtB/DNA complex (dashed grey line).

the tripartite complex [Fig. 6(A)], which are well maintained during the MD simulations. The stability of the active site hydrogen-bonding network in the holotoxin is critical to the auto-inhibition and DNA catalysis. When CdtB is disassembled from the complex, most of these active site residues exhibit high flexibility, and the hydrogen-bonding network is mostly disrupted. In the case of DNA binding, however, a number of hydrogen bonds are formed between the DNA and residues Arg144, Arg117, His274, His160, and water-mediated hydrogen bonds with residues D238 and Asn201 [Fig. 6(B)]. This rearranged hydrogen-bonding network in the CdtB-DNA complex is also well maintained over the MD simulations.

Dynamics of the Heterodimeric Sub-complexes

The RMSD plots of the three separate heterodimeric sub-complexes of CdtA-CdtB, CdtA-CdtC, and CdtB-

CdtC show considerably increased flexibility during the course of MD simulations as compared to those in the tripartite form (see Fig. 7). The mobile regions mainly involve the exposed binding interface and are caused by the disassociation from the tripartite complex. CdtB is generally stable in the two sub-complexes with CdtA and CdtC during the simulations. Conformational changes are found with the closure of the DNA binding groove in the CdtB-CdtA sub-complex, as observed in free CdtB due to the absence of the CdtC N-terminal peptide binding. The heterodimeric CdtA-CdtC complex shows large RMSDs compared to the CdtA-CdtB and CdtB-CdtC sub-complexes. One reason is that the long peptide tail of the CdtC N-terminus is disassembled from the DNA binding site of CdtB and becomes highly flexible. To further detect localized structural conformational changes, the atomic fluctuations of $C\alpha$ atoms of CdtA and CdtC calculated from the tripartite and heterodimeric complexes were compared with experimental B-factors. As shown in Figure 8, the overall trends of calculated and the experimentally measured B-factors in the tripartite complex are in agreement with correlation coefficients of ~ 0.81 . However, remarkably increased fluctuations are observed with a number of regions in the disassembled CdtA-CdtC sub-complex. Most of these regions are specifically associated with the aromatic patch and loops surrounding the groove, the two characterized structural elements on CdtA and CdtC protein surface that are hypothesized to play an important role in receptor binding.^{11,17} Residues in the CdtA-CdtC binding interface such as Met81, Tyr211, and Gln83, which contribute to the formation of the groove, also show high mobility as compared to those in the tripartite complex.

The increased flexibility and dynamics changes of the separate sub-complexes suggest that these heterodimers are not as stable alone as they are in the tripartite complex. An analysis of interactions between CdtA and CdtC reveals that the binding is characterized by non-polar, hydrophobic interactions as well as a number of hydrogen bonds across the binding interface. CdtB apparently

plays a stabilizing role in the interactions with both CdtA and CdtC in the tripartite complex by forming extensive polar and non-polar interactions. Table I shows the hydrogen bonds with their percentage of occurrence during the 10 ns of MD simulations for the separate CdtA-CdtC and in the tripartite complex. Most of these hydrogen bonds are found to be rather stable throughout the simulations in the tripartite complex, but many are decreased significantly in the separate heterodimeric complex, revealing reduced stability in these regions due to the disassembly from the tripartite complex. One exception is the well-defined H-bonding network at the intermolecular β -sheet region of CdtA C-terminus, which is also well maintained in the separate heterodimers. Comparative structural analysis shows that the intermolecular β -sheet region is the highest conserved region among different CdtA and CdtC species.⁴⁰ The high stability of these intermolecular β -sheet interactions indicates that they are a major stabilizing force for the assembly of CdtA-CdtC complex. Interestingly, the hydrogen bond between the backbone oxygen of Gln83 (CdtA) and Arg43 (CdtC) appears to be rather stable in the separate CdtA-CdtC complex, although the

side chains of these polar residues are found to be highly flexible in both tripartite and heterodimeric complexes. Experiments reveal that the crystal-packing molecule of CdtA N-terminal peptide inserts into the groove to interact with residues Arg43 and Gln83.¹⁷ Both Gln83 and Arg43 are located at the bottom of the characterized groove on CdtA and CdtC protein surface and play an important role in maintaining the integrity of the groove, which is critical to its functional role in substrate binding for the intracellular delivery of active subunit CdtB.

Correlated Motions in the CDT Tripartite Complex

We performed cross-correlation analysis of the atomic fluctuations from the MD simulations to further probe the correlated motions of residues and long-range interplay between subunits in the CDT holotoxin. The DCCM of CDT, calculated between motions of $C\alpha$ atoms and averaged over an interval of 2–10 ns time course of the MD simulations, is depicted in Figure 9(A). The diagonally symmetric map quantifies the concerted motions of the binding subunits with respect to each other in the tripartite complex. The correlation values vary in the range between -1 (dark blue) and 1 (dark red). Positive correlations usually involve neighboring groups and contiguous loops, which move in the same direction. Negative anti-correlations indicate motions in opposing direction. Correlated and anti-correlated motions also occur among distant regions involving domain–domain communications. A completely correlated (1) or anti-correlated motion (-1) means the motions have the same phase and period. A value of zero (green) indicates uncorrelated motions.

Analysis of the DCCM of the CDT holotoxin shows that CdtA is anti-correlated to CdtC, while both CdtA and CdtC present weakly anti-correlated motions with CdtB [Fig. 9(A)]. It is apparent that strongly correlated motions are dominant within subunit domains, especially in CdtA and CdtC; whereas anti-correlated motions mainly occur between subunits with respect to

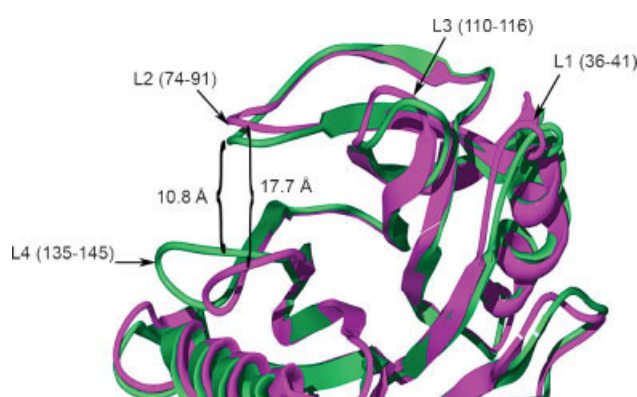


Fig. 5. Superimposition of the crystal structure of CdtB in the bound tripartite complex (purple) and the average MD structure (unbound) over the last 8 ns of simulations. The loops around the DNA binding site are indicated. The labeled distances are calculated between the $C\alpha$ atoms of Gly85 (L2) and Val141 (L4).

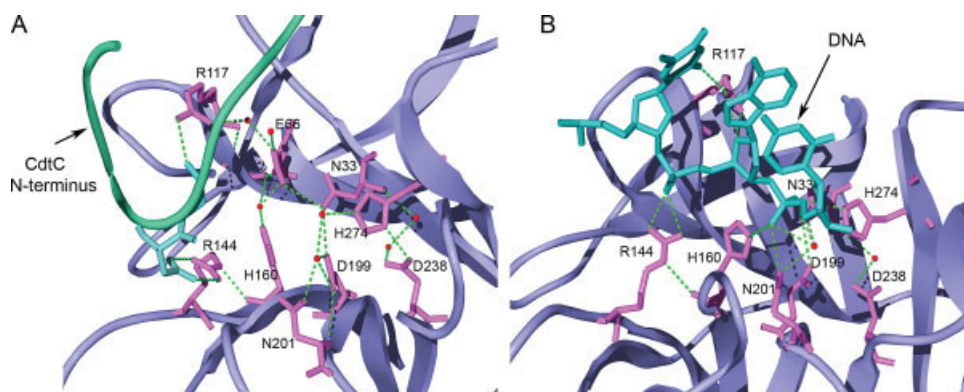


Fig. 6. Hydrogen-bonds at the active site of CdtB in (A) the tripartite complex and (B) the modeled CdtB-DNA complex.

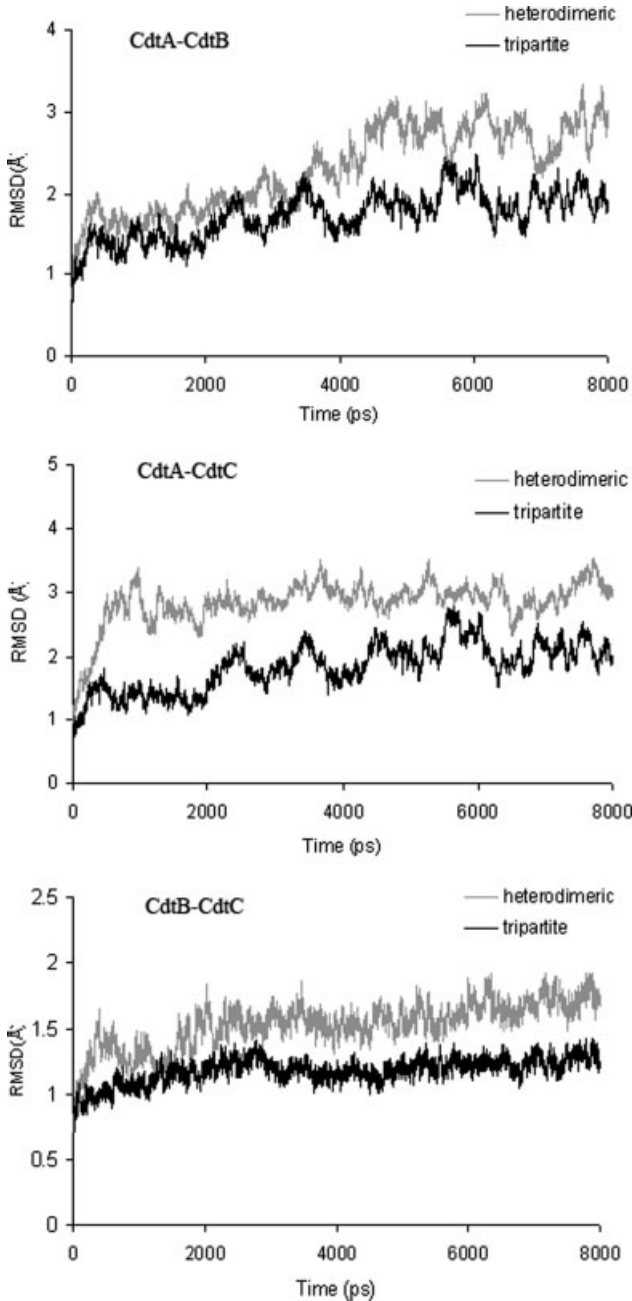


Fig. 7. RMSD plots of the heterodimeric sub-complexes of CdtA-CdtB, CdtA-CdtC, and CdtB-CdtC during the simulations as compared to the dynamics in the tripartite complex.

each other. The extensive correlated motions are related to the subunit interactions in the CDT tripartite complex. It is of interest to note the positive correlations across the terminal binding interface. The N-terminus of CdtC is significantly correlated with residues spanning 253–257, 282–284, and 310–312, which correspond to the active site residues as highlighted by squares in Figure 9(A) (the CdtB sequence number 87–91, 116–118, and 144–146). The same correlated motions are observed for the DNA bound to CdtB, reflecting the coupled move-

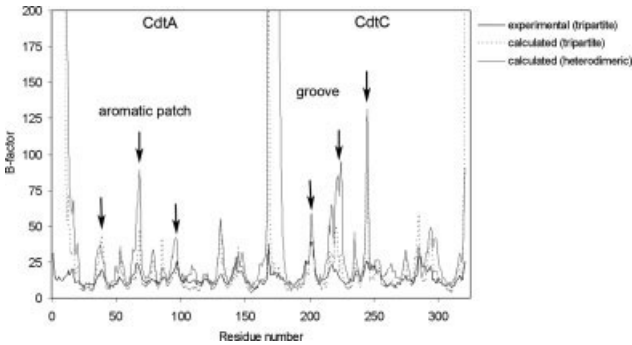


Fig. 8. Calculated B-factors of C α atoms of heterodimeric complex CdtA-CdtC (solid grey line) and the dimeric form in the tripartite complex (dashed grey line). The B-factors obtained from experimental X-ray structure are shown in solid black line.

TABLE I. Hydrogen Bonds Across the CdtA-CdtC Interaction Interface with Their Percentage of Occurrence During 10 ns MD Simulations

Hydrogen-bonds		Tripartite		Heterodimeric	
CdtA	CdtC	%	Distance	%	Distance
V222NH	P119O	99.84	2.89 \pm 0.12	99.68	2.91 \pm 0.13
L217O	Q163NH	99.53	2.91 \pm 0.14	98.85	2.94 \pm 0.15
A219O	F158NH	99.25	2.94 \pm 0.14	99.51	2.92 \pm 0.13
A221NH	R156O	98.74	3.02 \pm 0.16	99.30	3.01 \pm 0.15
T220NH	N121OD	97.95	2.94 \pm 0.15	95.83	2.98 \pm 0.17
A221O	G155NH	94.72	3.01 \pm 0.18	93.92	2.95 \pm 0.17
P163O	L176NH	88.20	3.08 \pm 0.17	49.25	2.97 \pm 0.15
P71O	N121NH	85.40	3.03 \pm 0.18	32.25	3.07 \pm 0.19
Q83NH	G171O	67.67	2.98 \pm 0.17	45.86	3.09 \pm 0.19
N223NH	D81O	54.79	2.89 \pm 0.14	28.54	2.86 \pm 0.13
Q83O	R43NH	43.01	2.94 \pm 0.18	83.93	2.99 \pm 0.18
N104NH	L46O	22.07	3.05 \pm 0.20	5.77	3.13 \pm 0.21
Y211O	R43NH	18.82	3.16 \pm 0.18	5.32	3.19 \pm 0.13
D165O	K174NH	2.53	3.01 \pm 0.18	0.47	3.09 \pm 0.23

ments of the substrate with CdtB at the active site. Another group displaying highly correlated motions was found with the C-terminal end of CdtA spanning residues 523–525 and 558–564 (corresponding to the CdtC residues 119–121 and 154–160), indicating the close interplay between CdtA and CdtC at the intermolecular β -sheet interaction region of these two lectin-like domains.

The DCCMs of CdtB in the tripartite complex were also compared to the DCCM obtained from separate simulations. In this case, the CdtB protein is superimposed only on the corresponding partner in the tripartite complex, the relative motions between subunits with respect to each other are not included, therefore, revealing changes of proteins in internal motions due to complex formation. As shown in Figure 9(B), the correlated motions involving the CdtB subunit are very different in the unbound and bound states. While the concerted motions are generally weak in the tripartite complex, correlated and anti-correlated motions become more pro-

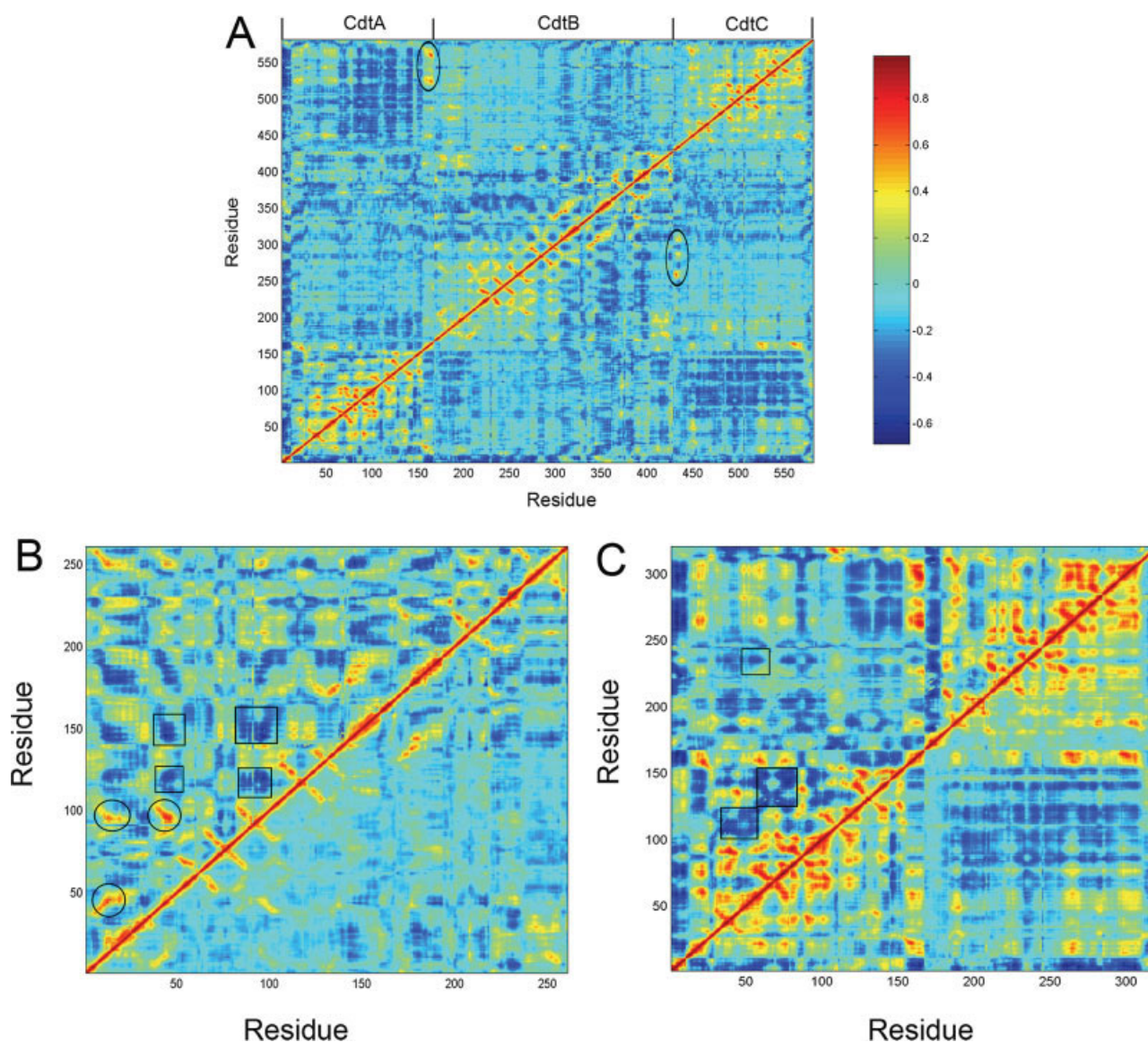


Fig. 9. DCCM of C_{α} atomic fluctuations of (A) the CDT tripartite complex, (B) unbound CdtB, and (C) CdtA-CdtC sub-complex. The diagram is diagonally symmetric in (A). In (B) and (C), the correlations for unbound CdtB and separate CdtA-CdtC are shown in the upper left triangle, while the correlations for the bound protein in the tripartite complex are shown in the lower right triangle. In the latter case, the molecule was superimposed only onto the corresponding protein in the tripartite complex. Residues with characterized correlated and anti-correlated motions are marked with black circles and squares and discussed in the text.

nounced in unbound CdtB. Strongly correlated motions emerge in the regions spanning residues 14–19, 45–50, and 90–100 (corresponding to the CdtB sequence number 36–41, 67–72, and 112–122). Highly anti-correlated motions are observed for the regions spanning residues 88–95 and 145–150 (CdtB sequence numbering 110–117 and 167–172) with residues 14–19 and 45–50 (CdtB sequence numbering 36–41, 67–72). These regions, highlighted by black circles and squares in Figure 9(B), are mostly identified as spatially adjacent loops including L1–L4 in the vicinity of DNA binding site. These strongly coupled movements reveal the changes in the

DNA binding site of CdtB upon disassembled from CdtA and CdtC.

The influence of complex formation on the internal motions appears to be more intense for the CdtA-CdtC sub-complex. Figure 9(C) shows the concerted motions within the CdtA-CdtC sub-complex as compared to the movements in the tripartite complex. A striking difference in the heterodimer complex is that CdtA exhibits increased anti-correlated motions, mainly involving the residues of the aromatic patch on the protein surface [such as residues 42, 44, 50, 133, 144, and 232, Fig. 9(C)]. These face-to-face clustering aromatic residues are

TABLE II. Binding Free Energies of CdtA-CdtB, CdtA-CdtC, and CdtB-CdtC Sub-complexes Calculated by MM-GBSA from Snapshots Extracted from Separate and Complex Simulation Trajectories^a

Cont. ^b	Separate sub-complex ^c			Tripartite complex ^c		
	CdtA-CdtC	CdtB-CdtA	CdtB-CdtC	CdtA-CdtC	CdtB-CdtA	CdtB-CdtC
ΔE_{elec}	-85.19	-231.54	-226.98	-95.85	-252.60	-243.28
ΔE_{vdw}	-192.11	-132.59	-164.32	-193.94	-136.81	-162.03
ΔE_{int}	0.01	0.01	0.01	0.01	0.01	0.01
ΔE_{gas}	-277.29	-364.12	-391.29	-289.78	-389.41	-405.29
ΔG_{nonpol}	-19.96	-16.56	-19.38	-20.62	-17.24	-19.05
ΔG_{GB}	177.18	322.08	317.97	177.15	336.71	315.99
ΔG_{sol}	157.22	305.53	298.59	156.52	319.47	296.94
$\Delta G_{\text{subtotal}}$	-120.06	-58.59	-92.70	-133.25	-69.94	-108.35
$T\Delta S$	-84.09	-53.86	-77.42	-85.75	-57.79	-84.97
ΔG_{total}	-35.97	-4.73	-15.28	-47.50	-12.15	-23.38

^aAll value are given in kcal/mol.

^b $\Delta E_{\text{gas}} = \Delta E_{\text{elec}} + \Delta E_{\text{vdw}} + \Delta E_{\text{int}}$; $\Delta G_{\text{sol}} = \Delta G_{\text{GB}} + \Delta G_{\text{nonpol}}$; $\Delta G_{\text{subtotal}} = \Delta E_{\text{gas}} + \Delta G_{\text{sol}}$; $\Delta G_{\text{total}} = \Delta G_{\text{subtotal}} - T\Delta S$.

^cThe free energy components of each subunit and heterodimer in different complex systems and the calculations of binding free energies are shown in supplementary materials (Table S1–S4).

observed mainly with strong correlated motions in the tripartite complex simulations. Residues across the interaction interface also show a high level of anti-correlated motions, in contrast to the major correlated motions in the tripartite complex. The different dynamical behaviors of these structurally important residues, especially associated with the aromatic patch and the groove in CdtA and CdtC, are apparently caused by the third partner of CdtB bound to the two lectin domains in the holotoxin.

Cooperation of Subunit Interactions in the Tripartite Complex

To investigate the stability and energetics within protein–protein interactions of CDT subunits binding free energies were calculated applying the MM-GBSA method based on the generalized Born model of Onufriev et al.³⁸ The absolute free energies were obtained as averaged over 150 snapshots taken at 20 ps intervals from the last 3 ns of MD simulations, and the binding free energies of CdtA-CdtC, CdtB-CdtA, and CdtB-CdtC were calculated by the free energy differences between the heterodimeric complexes and their respective subunits. To ensure reliable estimates of binding free energies, we examined the energy fluctuations along the trajectories used for the MM-GBSA calculations. The sum of gas-phase energies and solvation free energies is plotted as a function of time for snapshots of the three sub-complexes obtained from the separate heterodimeric and tripartite complex simulations (Supplementary Table S1–S4). Although the total energies still exhibit significant oscillations over the time course, the mean values remain rather stable for all the simulation systems. These plots suggest that the average values of the total energies have reasonably converged throughout the trajectories.

The binding free energies of the three subunit interactions of CdtA-CdtC, CdtB-CdtA, and CdtB-CdtC ob-

tained from the separate heterodimeric complex simulations are shown in Table II. The results reveal that the estimated binding affinities of CdtA and CdtC are much higher than those of CdtB bound with CdtA or CdtC, respectively, and CdtB binds to CdtC more tightly than CdtB-CdtA sub-complex. This is in good agreement with experimental observations. Shenker et al. investigated the association of the three CDT subunits from *A. actinomycetemcomitans* using an optical biosensor technology.¹⁴ One of the subunits was immobilized to a sensor chip and another subunit was added to allow a direct examination of the complex formation and binding affinities. The results have shown that CdtA and CdtC are capable of forming a stable complex with a binding affinity of $2.3 \times 10^{-7}M$, but the binding of CdtB with either CdtA or CdtC was not detected. Other studies have also shown that the combination of purified CdtB with CdtC is slightly cytotoxic, whereas no cytotoxic effect has been observed for the combination of CdtA and CdtB.^{12,41} These experimental results have suggested that CdtC alone may be able to bind with CdtB, albeit weakly, to achieve toxicity, whereas interactions of CdtA with CdtB are too weak to do so. Comparative structural analysis also reveals that CdtC is more conserved than CdtA in the binding interface with CdtB among the CDT family.⁴⁰ On the other hand, a relatively weak binding affinity of CdtB to both CdtA and CdtC compared to the two-lectin domains binding to each other may help in complex disassembly during intracellular delivery.

We also calculated the binding free energies of the three CDT subunit interactions in the tripartite complex. Snapshots of the heterodimeric sub-complexes of CdtA-CdtB, CdtA-CdtC, and CdtB-CdtC were extracted directly from the trajectory of CDT simulations and binding free energies were calculated using MM-GBSA. Again, the interactions of CdtA and CdtC with each other are stronger than their individual binding to CdtB, with the binding affinity of CdtB-CdtC higher than that of CdtB-CdtA (Table II). Notably, the estimated binding

free energies of the three subunit interactions from the tripartite complex are significantly lower as compared to the binding free energies obtained from the separate heterodimeric sub-complex simulations. This raises an interesting issue that interactions of CdtA, CdtB, and CdtC subunits in the tripartite complex might differ from the binding in the disassembled complexes. Consistent with the increased stability of the heterodimers observed in the simulations, the three subunits in the tripartite complex likely bind in a cooperative manner so that the binding affinities of CdtA-CdtC, CdtB-CdtA, and CdtB-CdtC are enhanced by the third subunit participation upon tripartite complex formation.

To further examine the subunit interactions and contributions of binding free energy in the tripartite complex, we analyzed the energy decomposition with MM-GBSA calculations to partition the gas-phase energies and solvation free energies ($\Delta G_{\text{gas} + \text{sol}}$) between residues of both binding partners. Figure 10 depicts the energy contributions of some structurally important residues to the three subunit interactions in the CDT complex. Most of these identified structural determinants ("binding epitope") are located at the interaction interfaces of both binding partners. In CdtB binding to CdtC, electrostatic interactions are favorable in complex formation, opposed by unfavorable contributions due to the polar part of the solvation free energy. In contrast, the van der Waals interactions contribute more favorably to the binding affinity of CdtA-CdtC formation, as does the non-polar part of solvation free energy. It is worth noting that a number of residues contribute greatly in both subunit interactions. For example, CdtB Gln269 forms hydrogen bonds with CdtA Ser166 as well as with CdtC Arg39 and contributes 4.46 and 1.57 kcal/mol to the binding of CdtB-CdtA and CdtB-CdtC, respectively. CdtC Pro119 participates in extensive hydrophobic interactions with Val222 and Ala221 in CdtA, as well as with Asn46 and Arg50 in CdtB. These common binding epitopes appear to play a key role in tripartite complex assembly, and their loss during disassembly would destabilize the remaining sub-complex formation. In fact, not only the binding epitopes across the binding interface, but also residues apart from the interface contribute significantly to the subunit interactions in the tripartite complex, and overall, the optimal assembly is achieved with the presence of all the three subunits.

We should point out that accurate calculation of absolute binding free energy of biomolecular complex still remains a challenging problem, although progress has been made recently.^{42,43} The MM-GBSA method represents a promising approach combining physics-based energy function with implicit continuum solvent model to treat the solvation effects, but it is limited by a number of approximations. As shown in this study for the calculations of binding free energies of the three CDT subunit interactions, the binding affinities of the CdtA-CdtC complex appear to be overestimated. Given the complexity of the CDT tripartite system and the magnitude of the molecular interactions involved, such dis-

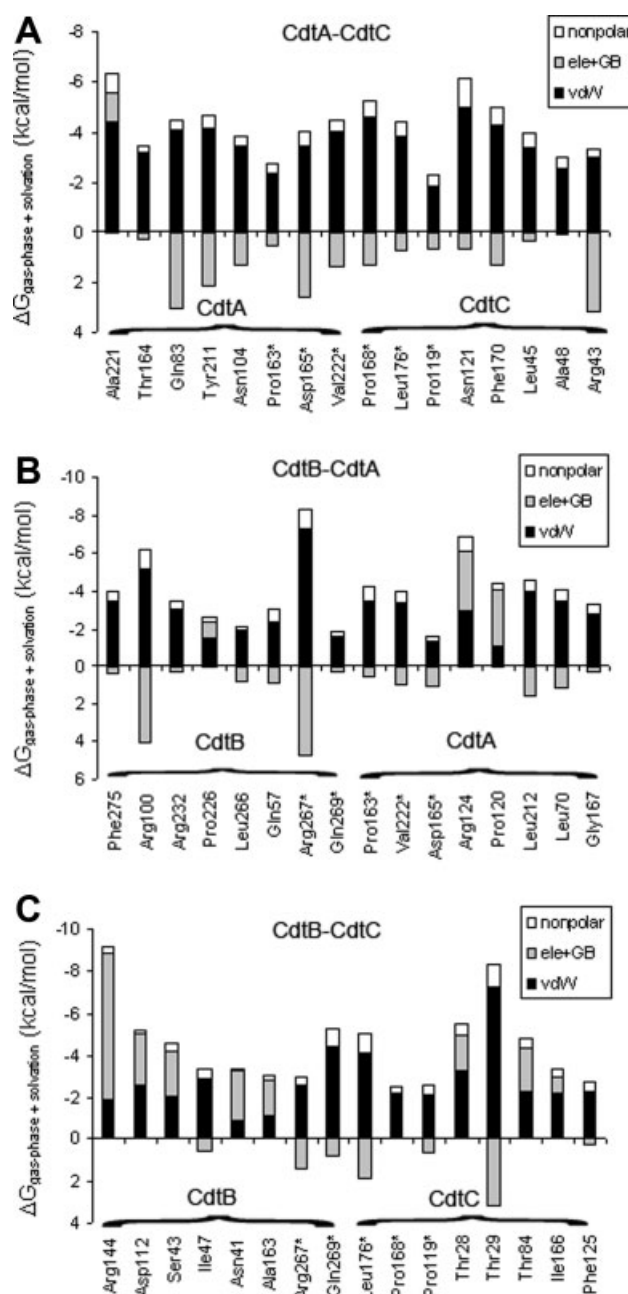


Fig. 10. Contributions of the binding free energy ($\Delta G_{\text{gas} + \text{sol}}$) of interfacial residues identified in the three subunit interactions of (A) CdtA-CdtC, (B) CdtB-CdtA, and (C) CdtB-CdtC in the tripartite complex. The residues involving in both sub-complex interactions are marked with an asterisk.

crepancies of estimated binding free energies are not unexpected. The promising result in this present study is that the relative binding affinities of the three subunit interactions predicted by MM-GBSA are consistent with experimental observations. More interestingly, the binding affinities of sub-complexes in the tripartite complex are significantly higher than those in the separate state, providing some insight into the nature of CDT subunit

interaction in the CDT assembly, namely, that the three CDT subunits bind to each other in a cooperative manner to achieve high stability and maximum activity of the holotoxin.

CONCLUSIONS

We have investigated the dynamics and assembly of the CDT holotoxin and subunit interactions using MD simulations and binding free energy calculations. The active subunit CdtB is found to undergo significant conformational changes when disassembled from the tripartite complex, and the active site likely adopts a more stable conformation with a closed DNA binding site in the unbound state. The sub-complexes of CdtA-CdtC, CdtB-CdtA, and CdtB-CdtC in the disassembled state exhibit markedly increased flexibility as compared with the tripartite complex, indicating that these separate heterodimers are less stable. Complex formation causes the internal motions of residues among subunit proteins to be more correlated, especially for the aromatic patch and the groove on the CdtA and CdtC protein surface that may have implications for their potential role in receptor binding. In agreement with experimental data, our estimated binding free energies have shown that the two lectin domains of CdtA and CdtC bind to each other with high affinities, but possess weaker interactions with CdtB if bound separately. The binding affinities of the three subunit interactions in the tripartite complex are much higher than those in the disassembled heterodimeric sub-complexes, underscoring the cooperative interactions of subunits in the tripartite complex. These results provide a better understanding of the assembly, stability, and related functional aspects of the CDT holotoxin at the atomic level that should serve as a guide for further experimental and mutagenesis studies.

ACKNOWLEDGMENTS

The authors thank R. Bennett, C. Pepper, A. Gazes, and G. Latter of the Rockefeller University Information Technology Resource Center for computational facilities.

REFERENCES

- De Rycke J, Oswald E. Cytolethal distending toxin (CDT): a bacterial weapon to control host cell proliferation? *FEMS Microbiol Lett* 2001;203:141–148.
- Frisan T, Cortes-Bratti X, Thelestam M. Cytolethal distending toxins and activation of DNA damage-dependent checkpoint responses. *Int J Med Microbiol* 2002;291:495–499.
- Lara-Tejero M, Galan JE. Cytolethal distending toxin: limited damage as a strategy to modulate cellular functions. *Trends Microbiol* 2002;10:147–152.
- Thelestam M, Frisan T. Cytolethal distending toxins. *Rev Physiol Biochem Pharmacol* 2004;152:111–133.
- Shenker BJ, McKay T, Datar S, Miller M, Chowhan R, Demuth D. *Actinobacillus actinomycetemcomitans* immunosuppressive protein is a member of the family of cytolethal distending toxins capable of causing a G(2) arrest in human T cells. *J Immunol* 1999;162:4773–4780.
- Purdy D, Buswell CM, Hodgson AE, McAlpine K, Henderson I, Leach SA. Characterisation of cytolethal distending toxin (CDT) mutants of *Campylobacter jejuni*. *J Med Microbiol* 2000;49:473–479.
- Young VB, Knox KA, Pratt JS, Cortez JS, Mansfield LS, Rogers AB, Fox JG, Schauer DB. In vitro and in vivo characterization of *Helicobacter hepaticus* cytolethal distending toxin mutants. *Infect Immun* 2004;72:2521–2527.
- Pickett CL, Cottle DL, Pesci EC, Bikah G. Cloning, sequencing, and expression of the *Escherichia coli* cytolethal distending toxin genes. *Infect Immun* 1994;62:1046–1051.
- Lara-Tejero M, Galan JE. CdtA, CdtB, and CdtC form a tripartite complex that is required for cytolethal distending toxin activity. *Infect Immun* 2001;69:4358–4365.
- Lara-Tejero M, Galan JE. A bacterial toxin that controls cell cycle progression as a deoxyribonuclease I-like protein. *Science* 2000;290:354–357.
- Nesic D, Stebbins CE. Mechanisms of assembly and cellular interactions for the bacterial genotoxin CDT. *PLoS Pathog* 2005;1:e28.
- Lee RB, Hassane DC, Cottle DL, Pickett CL. Interactions of *Campylobacter jejuni* cytolethal distending toxin subunits CdtA and CdtC with HeLa cells. *Infect Immun* 2003;71:4883–4890.
- Shenker BJ, Besack D, McKay T, Pankoski L, Zekavat A, Demuth DR. *Actinobacillus actinomycetemcomitans* cytolethal distending toxin (Cdt): evidence that the holotoxin is composed of three subunits: Cdt A, Cdt B, and Cdt C. *J Immunol* 2004;172:410–414.
- Shenker BJ, Besack D, McKay T, Pankoski L, Zekavat A, Demuth DR. Induction of cell cycle arrest in lymphocytes by *Actinobacillus actinomycetemcomitans* cytolethal distending toxin requires three subunits for maximum activity. *J Immunol* 2005;174:2228–2234.
- Cortes-Bratti X, Chaves-Olarte E, Lagergard T, Thelestam M. Cellular internalization of cytolethal distending toxin from *Haemophilus ducreyi*. *Infect Immun* 2000;68:6903–6911.
- Alby F, Mazars R, de Rycke J, Guillou E, Baldin V, Darbon JM, Ducommun B. Study of the cytolethal distending toxin (CDT)-activated cell cycle checkpoint. Involvement of the CHK2 kinase. *FEBS Lett* 2001;491:261–265.
- Nesic D, Hsu Y, Stebbins CE. Assembly and function of a bacterial genotoxin. *Nature* 2004;429:429–433.
- Kollman P. Free-energy calculations—applications to chemical and biochemical phenomena. *Chem Rev* 1993;93:2395–2417.
- Wang W, Donini O, Reyes CM, Kollman PA. Biomolecular simulations: recent developments in force fields, simulations of enzyme catalysis, protein-ligand, protein-protein, and protein-nucleic acid noncovalent interactions. *Annu Rev Biophys Biomol Struct* 2001;30:211–243.
- Honig B, Nicholls A. Classical electrostatics in biology and chemistry. *Science* 1995;268:1144–1149.
- Srinivasan J, Cheatham TE, Cieplak P, Kollman PA, Case DA. Continuum solvent studies of the stability of DNA, RNA, and phosphoramidate–DNA helices. *J Am Chem Soc* 1998;120:9401–9409.
- Massova I, Kollman PA. Computational alanine scanning to probe protein-protein interactions: a novel approach to evaluate binding free energies. *J Am Chem Soc* 1999;121:8133–8143.
- Kollman PA, Massova I, Reyes C, Kuhn B, Huo S, Chong L, Lee M, Lee T, Duan Y, Wang W, Donini O, Cieplak P, Srinivasan J, Case DA, Cheatham TE, III. Calculating structures and free energies of complex molecules: combining molecular mechanics and continuum models. *Acc Chem Res* 2000;33:889–897.
- Weston SA, Lahm A, Suck D. X-ray structure of the DNase I-d(GGTATACC)2 complex at 2.3 Å resolution. *J Mol Biol* 1992;226:1237–1256.
- SYBYL Molecular Modelling Software, v7.0; Tripos Associates, St. Louis, MO.
- Powell MJD. Restart procedures for the conjugate gradient method. *Math Programming* 1977;12:241–254.
- Case DA, Darden TA, Cheatham TE, III, Simmerling CL, Wang J, Duke RE, Luo R, Merz KM, Wang B, Pearlman DA, Crowley M, Brozell S, Tsui V, Gohlke H, Mongan J, Hornak V, Cui G, Beroza P, Schafmeister C, Caldwell JW, Ross WS, Kollman PA. AMBER 8, University of California, San Francisco; 2004.
- Jorgensen WL, Chandrasekhar J, Madurs J, Impey RW, Klein ML. Comparison of simple potential functions for simulating liquid water. *J Chem Phys* 1983;79:926–935.

29. Ryckaert JP, Ciccotti G, Berendsen JC. Numerical integration of the cartesian equation of motion of a system with constraints: molecular dynamics of *n*-alkanes. *J Comput Phys* 1977;23:327–341.
30. Darden T, York D, Pedersen L. Particle mesh Ewald—an $N \log(N)$ method for Ewald sums in large systems. *J Chem Phys* 1993;98:10089–10092.
31. Berendsen HCJ, Postma JPM, van Gunsteren WF, DiNole A, Haak JR. Molecular dynamics with coupling to an external bath. *J Chem Phys* 1984;81:3684–3690.
32. McCammon JA, Harvey SC. Dynamics of proteins and nucleic acids. Cambridge, UK: Cambridge University Press; 1987.
33. Ichiye T, Karplus M. Collective motions in proteins—a covariance analysis of atomic fluctuations in molecular-dynamics and normal mode simulations. *Proteins* 1991;11:205–217.
34. Tsui V, Case DA. Calculations of the absolute free energies of binding between RNA and metal ions using molecular dynamics simulations and continuum electrostatics. *J Phys Chem B* 2001;105:11314–11325.
35. Gohlke H, Kiel C, Case DA. Insights into protein-protein binding by binding free energy calculation and free energy decomposition for the Ras-Raf and Ras-RalGDS complexes. *J Mol Biol* 2003;330:891–913.
36. Gohlke H, Case DA. Converging free energy estimates: MM-PB(GB)SA studies on the protein-protein complex Ras-Raf. *J Comput Chem* 2004;25:238–250.
37. Lee MC, Yang R, Duan Y. Comparison between Generalized-Born and Poisson-Boltzmann methods in physics-based scoring functions for protein structure prediction. *J Mol Model* 2005;12:101–110.
38. Onufriev A, Bashford D, Case DA. Modification of the generalized Born model suitable for macromolecules. *J Phys Chem B* 2000;104:3712–3720.
39. Sanner MF, Olson AJ, Spehner JC. Reduced surface: an efficient way to compute molecular surfaces. *Biopolymers* 1996;38:305–320.
40. Hu X, Nesic D, Stebbins CE. Comparative structure-function analysis of cytolethal distending toxins. *Proteins* 2006;62:421–434.
41. Wising C, Svensson LA, Ahmed HJ, Sundaeus V, Ahlman K, Jonsson IM, Molne L, Lagergard T. Toxicity and immunogenicity of purified *Haemophilus ducreyi* cytolethal distending toxin in a rabbit model. *Microb Pathog* 2002;33:49–62.
42. Woo HJ, Roux B. Calculation of absolute protein-ligand binding free energy from computer simulations. *Proc Natl Acad Sci USA* 2005;102:6825–6830.
43. Lee MS, Olson MA. Calculation of absolute protein-ligand binding affinity using path and endpoint approaches. *Biophys J* 2006;90:864–877.